Fire Safety in Space – Investigating flame spread interaction over wires

Jean-Marie Citerne, Hugo Dutilleul, Koki Kizawa, Masashi Nagachi, Osamu
Fujita, Masao Kikuchi, Grunde Jomaas, Sébastien Rouvreau, Jose Torero,
Guillaume Legros

HAL Id: hal-01433528
https://hal.sorbonne-universite.fr/hal-01433528

Submitted on 12 Jan 2017

Fire Safety in Space – Investigating flame spread interaction over wires

Jean-Marie Citerne: Université Pierre-et-Marie Curie, Paris, France
Hugo Dutilleul: Université Pierre-et-Marie Curie, Paris, France
Koki Kizawa: Hokkaido University, Sapporo, Japan
Masashi Nagachi: Hokkaido University, Sapporo, Japan
Osamu Fujita: Hokkaido University, Sapporo, Japan
Masao Kikuchi: JAXA, Tsukuba, Japan
Grunde Jomaas: Technical University of Denmark, Kgs. Lyngby, Denmark
Sébastien Rouvreau: Belisama R&D, Toulouse, France
Jose L. Torero: University of Queensland, Brisbane, Australia
Guillaume Legros*: Université Pierre-et-Marie Curie-Paris6, Paris, France

Abstract

In order to reduce the uncertainty and risk in the design of spacecraft fire safety systems, a new experimental rig that allows the study of concomitant flames spreading over the coating of parallel cylindrical wires in an air flow parallel to the wires in microgravity has been developed. The parabolic flight experiments were conducted at small length- and timescales, i.e. typically over 10 cm long samples for up to 20 seconds. For the first time, the influence of neighboring spread on the mass burning rate was assessed in microgravity. The observations are contrasted with the influence characterized in normal gravity. The experimental results are expected to deliver meaningful guidelines for future, planned experiments at a larger scale.

Arising from the current results, the issue of the potential interaction among spreading flames also needs to be carefully investigated as this interaction plays a major role in realistic fire scenarios, and therefore on the design of the strategies that would allow the control of such a fire. Once buoyancy has been removed, the characteristic length and time scales of the different modes of heat and mass transfer are modified. For this reason, interaction among spreading flames may be revealed in microgravity, while it would not at normal gravity, or vice versa. Furthermore, the interaction may lead to an enhanced spread rate when mutual preheating dominates or, conversely, a reduced spread rate when oxidizer flow vitiation is predominant.

In more general terms, the current study supports both the SAFFIRE and the FLARE projects, which are large projects with international scientific teams. First, material samples will be tested in a series of flight experiments (SAFFIRE 1-3) conducted in Cygnus vehicles after they have undocked from the ISS. These experiments will allow the study of ignition and possible flame spread in real spacecraft conditions, i.e. over real length scale samples within real time scales. Second, concomitant research conducted within the FLARE project is dedicated to the assessment of new standard tests for materials that a spacecraft can be composed of. Finally, these tests aim to define the ambient conditions that will mitigate and potentially prohibit the flame spread in microgravity over the material studied.

I. Introduction

Long life power supplies are required for long term missions, such as the mission to Mars, therefore, hazards associated with short circuiting are enhanced. As a result, the control of potential flame spread over electrical wires is crucial to space vehicle fire safety. Managing this hazard requires the capacity to understand and predict the potential growth of a fire initiated by a short circuit. Only then, mitigation strategies can be implemented.

Following the pioneering works by Greenberg et al. [1], the characterization of flame spread over the coating of a single wire in microgravity has been studied extensively in recent years [2-9]. Thus, some governing processes have been identified [10], and it has been found that the "wire-driven mode" controls the spread rate over the coating of a high conductivity metallic core (Fe), while the spread rate follows a "flame-driven mode" for a low conductivity metallic core (Ni/Cr).

Due to the actual arrangements in spacecraft, some further issues arise, of which the most critical seem to be scale and interaction between burning wires. While the scale influence on fire spread is a topic extensively covered for both normal gravity and microgravity environments [11-13] it still remains unresolved. In a similar manner, the interaction among spreading flames has been the subject of several studies [13,14] but still merits further scientific investigation, in particular, for microgravity and low characteristic forced velocities conditions. The absence of natural convection allows a significant increase of the time scales associated with transport and combustion processes, increasing both soot concentration [15] and radiative emissions, especially from the soot continuum [16]. Transport thus changes the nature of the combustion processes and the interaction between the flame and the solid fuels in a manner that is still not fully understood. In microgravity, radiation from soot can then be the predominant mode of heat transfer involved in flame spread, even for small diffusion flames [17]. In a recent study, Olson [14] showed that the spread rates exhibited by two flames established in microgravity over parallel flat samples facing each other can be accelerated due to radiative heat transfer from every flame towards the opposite sample in spite of the oxidizer vitiation produced by the release of combustion products. However, for such a geometrical configuration, the optical access was restricted, and therefore it did not allow the sample mass burning rate to be quantified. Without the mass burning rate it is difficult to establish the interactions between the flame and the solid fuel.

This study follows the aforementioned studies by Fujita and coworkers [5-10,12] and focuses on the cable to cable interactions. While the main objective of understanding the influence of cable to

cable interactions on flame spread rates remains, the present paper documents a new experimental rig that has been custom-designed to conduct experiments in parabolic flights. The inner combustion chamber's aerodynamics was carefully characterized. Thus, flames spreading concomitantly over the polyethylene coatings of three parallel electrical wires were established in a uniform laminar oxidizer flow. A backlighting technique allowed the coating regression rates, therefore the mass burning rates to be quantified along the length of spread. The interaction among spreading flames was established by means of time histories of the mass burning rates in microgravity and normal gravity. This study therefore fills, for the first time in microgravity, a gap of information essential to the understanding of the interaction of spreading flames over adjacent cables.

II. Experimental Design

The experimental setup has been custom-designed to enable the study of flame spread over the coating of cylindrical wires in microgravity obtained through parabolic flights.

II.1. Configuration – Flame Spread

Figure 1 shows a schematic of a flame established over the coating of an electrical wire. For the present study, the 0.5 mm diameter metallic core was made of NiCr. The coating (outer diameter of 1.1 mm) was composed of polyethylene. Upon ignition of the coating, the flame may propagate over it, provided that the heat feedback from the flame to the coating enables the polyethylene pyrolysis. The mass transfer of this fuel pyrolyzate to the flame allows in turn the heat of combustion to be released at the flame location where the fuel meets the oxidizer. As indicated in Fig.1, different modes of heat and mass transfers may play significant roles in this coupling.

In the absence of buoyancy, the oxidizer will mainly be conveyed to the flame by advection. In a spacecraft, the forced flow advection is produced by a HVAC system, typically generating flows at velocities ranging from 1 to 10 cm/s. The corresponding range of Reynolds numbers typically leads to laminar oxidizer flows, as represented by the streamline shown in Fig.1. Although Fig.1 is schematic in nature, this streamline is in qualitative agreement with the computed streamlines in a similar configuration [18-20]. The streamline in Fig.1 conveys the oxidizer to the flame, before the combustion products are transported away from the flame. Due to this flow feature, the mass transfer of the fuel pyrolyzate is mainly attributed to molecular diffusion from the surface of the

coating to the flame. In addition, the heat feedback from the flame to the coating is governed by conduction and radiation, and the heat flux is partly used to preheat the coating.

Also, both conduction and radiation lead to heat losses as the flame and coating surface radiations are partly emitted to the surrounding while conduction allows heat dissipation, especially along the metallic core of the wire.

While the effect of the angle between the main flow direction and the burning surface normal can be questioned, the academic configuration represented in Fig.1 that sets both directions orthogonal remains meaningful. In such a configuration, a steady boundary layer can establish over the burning surface. This then allows analytical or semi-analytical models to be derived [21-24]. Furthermore, the effect of gravity on the potential interaction among flame spreads can be identified preserving the similarity of the main flow. Indeed, the rig outlined in the following enables the experiments to be conducted on vertical wires (see Fig.2). At normal gravity, buoyancy will still contribute to accelerate the main flow in regions where hot combustion products are released but will not affect the orientation of the boundary layer.

As the flame represented in Fig.1 spreads in the same direction as that of the oxidizer flow, this configuration is referred to the concurrent flame spread. Conversely, when the flame propagates in the opposite direction, the configuration is called opposed (or counter-current) flame spread and the spread rate is mainly controlled by the stabilization process at the leading edge of the flame [25]. On the other hand, the hot, still reacting combustion gases and particles that are produced along the concurrent flame spread are mainly moved downstream towards the pyrolysis front by forced convection. As a result, the radiative heat transfer to both the unburned material and the surrounding is enhanced. For this reason, the interaction among spreading flames is expected to be unveiled when investigating the concurrent flame spread configuration.
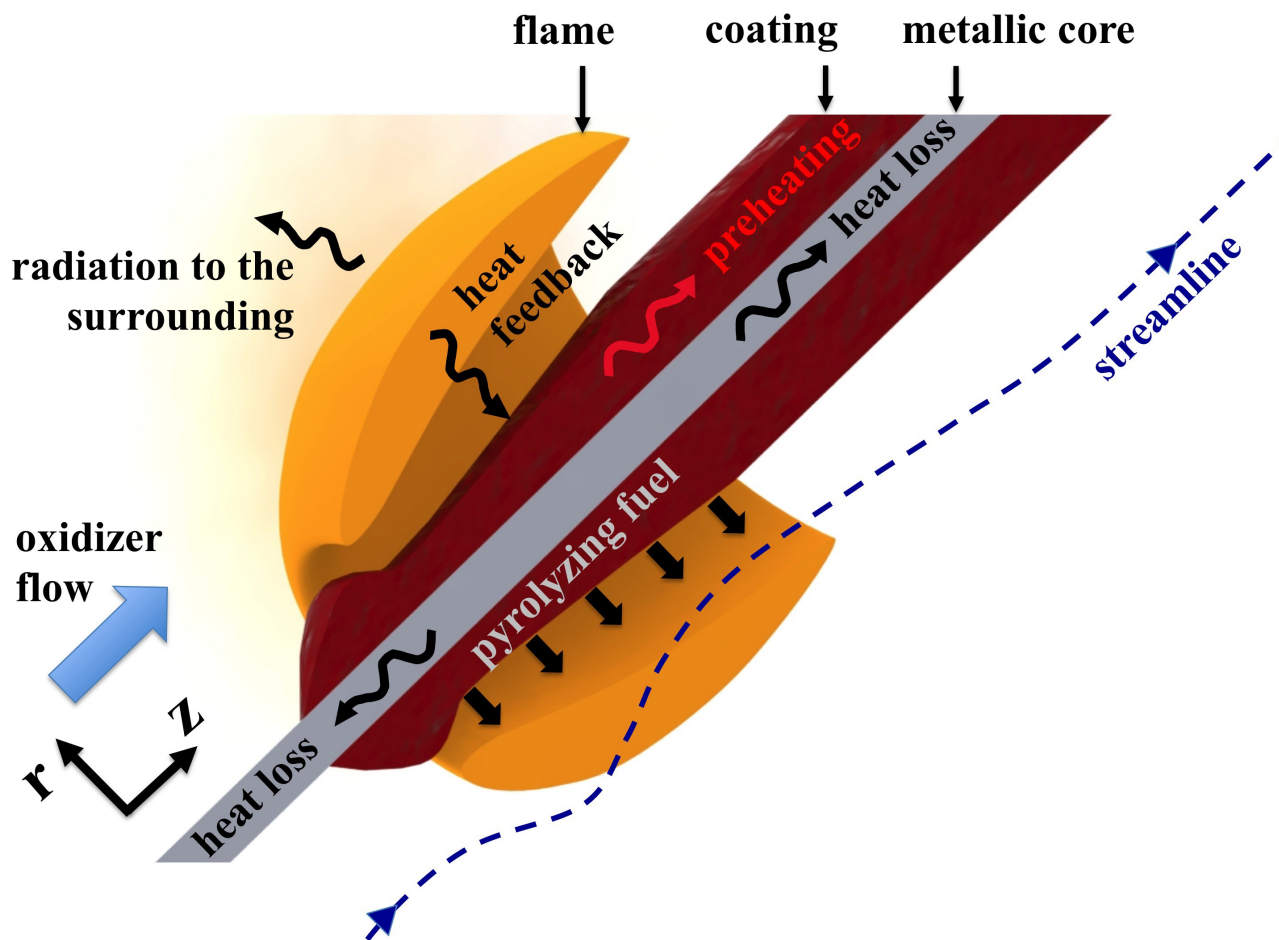
Figure 1: Schematic of the concurrent spread of a flame established over the polyethylene coating of a wire. The main heat and mass transfers are included.

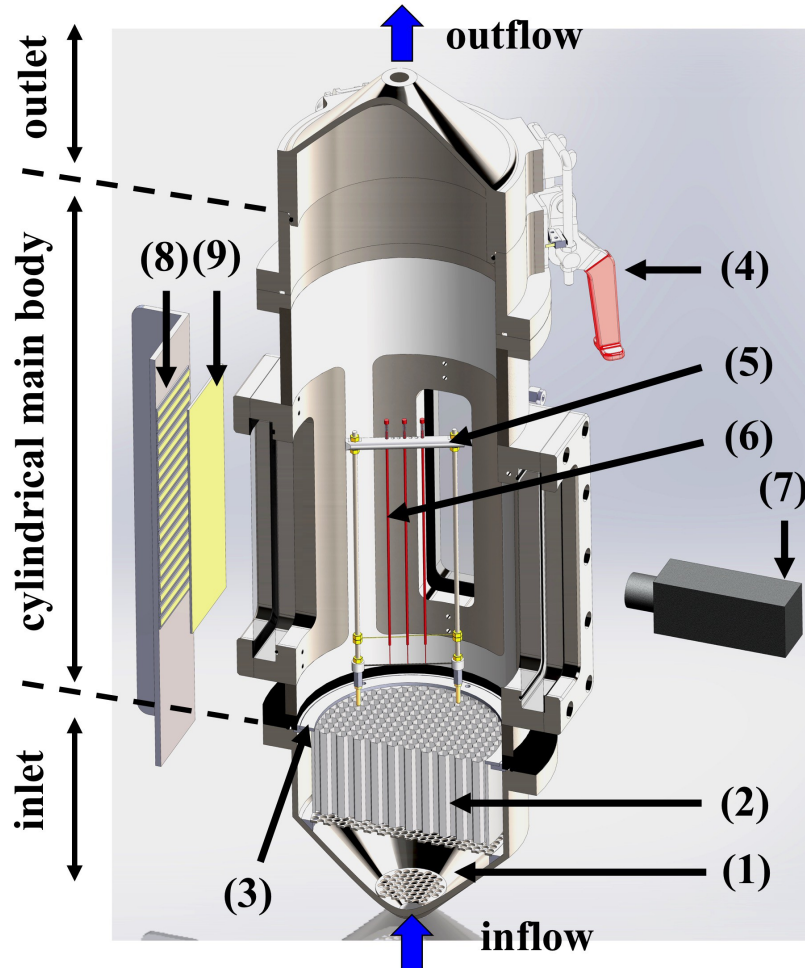**II.2. Control of the surrounding conditions**

Figure 2: Schematic of the combustion chamber designed for the parabolic flights. (1) Conical part filled with glass beads; (2) stainless steel honeycomb; (3) stainless steel ring; (4) latch clamp for top end locking; (5) sample holder; (6) polyethylene coated wires; (7) camera; (8) set of LEDs; (9) diffusive screen.

Oxidizer flow

Figure 2 shows the experimental arrangement in the combustion chamber, which allows for ignition and subsequent concurrent flame spread over a polyethylene coated wire. As outlined, the oxidizer flow plays a major role in this spread. Therefore, the preparation of this flow requires special attention.

To produce the oxidizer flow with different velocities and percentages of oxygen in nitrogen, nitrogen/oxygen mixtures with two different oxygen contents, namely 0% and 21%, were stored in high pressure cylinders. These were connected to a high pressure manifold that produced the in-line mixing. Two Bronkhorst mass flow controllers adjusted the flowrates from two cylinders with different oxygen contents. Thus, the downstream mixing of both flows allowed for control of both the oxygen content and the velocity of the oxidizer stream flowing towards the combustion

6

chamber. To overcome the potential fluctuations of ambient temperature and cooling due to gas expansion, the oxidizer flow temperature was controlled through the use of a heated line that connected the outlet of the mixing manifold to the inlet of the combustion chamber.

Upon entering the combustion chamber, the oxidizer flow is shaped so that it has a flat velocity profile at the leading edge of the unburned sample. As shown in Fig.2, the flow first enters the combustion chamber through a divergent piece into which glass beads with a 2 mm diameter homogenizes the flow over the cross section of the cylindrical part. A stainless steel honeycomb was placed at the inlet of this cylindrical part to ensure that the flow was laminar upon leaving this segment of the combustion chamber.

Extensive Computational Fluid Dynamics simulations performed with ANSYS Fluent [26] have driven the design of the inner combustion chamber. As a result, the 10 mm wide ring located at the outlet of the honeycomb was shown to constrain the development of the boundary layer at the wall. The cylindrical part with an inner diameter of 190 mm also allowed the core of the flow to be preserved from the perturbations associated with the windows, even in the presence of moderate gas expansion modeling the influence of the flame on the flow.

However, an experimental assessment of this design was required, in particular to evaluate the actual flow velocity as a function of the flowrate measured by the mass flow controllers. Therefore, one-component hot wire measurements were conducted in the absence of any wire. Figure 3 shows the evolution of the oxidizer velocity at the constant streamwise location z of the leading edge of the unburned coating as a function of the distance r from the chamber axis for three different steady flowrates. The ticks at r = ± 42 mm refer to the exact radial locations of the sample holder's lateral beams (see Fig.5). The markers indicate the locations of the measurements. For every flow rate, the uncertainty was evaluated as the maximum deviation from the mean values over the 10 s long recording sequence of every measurement. Among the three flow rates investigated, the maximum uncertainty was 1.7%. Consequently, the set of materials inserted at the chamber inlet is appropriate to provide a laminar flow of excellent quality with velocities ranging from 2 to 35 cm/s at the potential locations of the wires. Furthermore, the discrepancy between the numerical and experimental widths of the hydrodynamic boundary layer close to the wall supports the need for the experimental measurements. As a result of these measurements, it was found that the experimental flat profile region was more restricted than the numerical one. For this reason, every flow rate was adjusted experimentally to get the numerical velocity at r = 0, leading to an experimental flow rate higher than the predicted one.

Nevertheless, the experimental flat profile region remains large enough to allow multiple wire combustion to be conducted within a cautiously characterized homogeneous flow. In the central homogeneous region of 40 mm diameter, the velocity and the oxygen content can then be adjusted from 2 to 35 cm/s and from 0 to 21%, respectively.
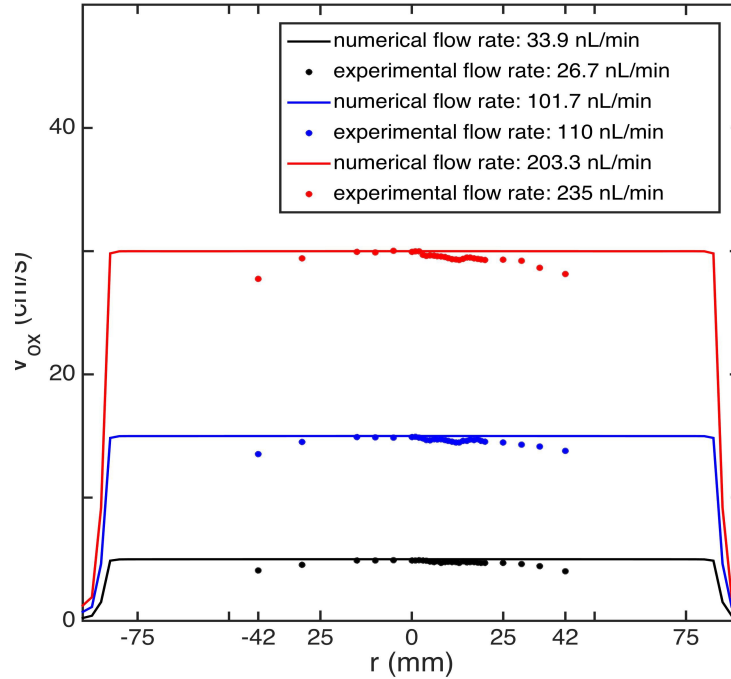

Figure 3: Computed (lines) and experimental (symbols) velocity profiles as a function of the distance, r, from the combustion chamber axis and at the constant axial location, z, from the leading edge of the coating.

Pressure

At the outlet of the combustion chamber, the exhaust gases flow through a metallic mesh grid that traps soot aggregates before the flow enter the exhaust line. The pressure regulation device was composed of a RCV control valve located along the exhaust line. This valve allows exhaust flow rates up to 1800 nL/min to be evacuated from the combustion chamber to the outside while the upstream pressure in the combustion chamber, as measured by a Keller pressure transmitter, was regulated at a stable pressure ranging from 0.8 to 1.5 bar. Due to the fluctuation of the outside pressure within a parabola (typically between 0.45 and 0.6 bar within the 22 s long duration of each flight parabola), a pneumatic actuator of the valve was selected and the adjustment of the proportional-integral-derivative controller parameters was given special attention. Along the parabolic flight campaign, for which results are reported in the present paper, the combustion chamber pressure could typically be established at a stable value typically 20 s after the oxidizer was introduced. This sequence was short enough to allow every single parabola to be exploited.

8

Moreover, within a parabola, the discrepancy between the setpoint and the actual combustion chamber pressure was lower than 0.01 bar.

Gravity

Microgravity conditions were obtained from parabolic flights on board of the Novespace A300 airplane. Figure 4 shows pictures of the rig on board the airplane. Extensive efforts were devoted to the certification of this rig, which was custom-made for parabolic flights. For safety reasons, all the flows had to be confined and ultimately released through the exhaust line, which was connected to the outside of the airplane. Furthermore, the mechanical requirements had to ensure that the rig's integrity would be preserved in case of an emergency landing leading to a deceleration of 9 g_0 . Due to these constraints, the rig consists of two racks. The combustion chamber, the optical diagnostics, the pressure regulation device, and the acquisition and control computer are located on the main rack (see Fig.4(b)). The removable top end of the combustion chamber was designed to allow the sequence of chamber opening, burned sample removal, new sample integration, and chamber closing to be operated between two consecutive parabolas. The inlet of the combustion chamber was connected to the secondary rack via the oxidizer line (see Fig.4(a)). This was dedicated to the oxidizer mixture preparation, and it therefore incorporates the bottles of compressed air and nitrogen together with the aforementioned mixing manifold.

Every parabola enables microgravity conditions with a quality of 10^{-2} g_0 for 22 s. This microgravity period was long enough to reach steady state conditions as evidenced by the pyrolysis rate time histories shown in Fig.8. The presence of g-jitter has an effect on the flame structure itself [18,19] that is difficult to quantify. However, Rouvreau et al. [18] have provided a numerical evaluation of the impact on the flow field, showing that high frequency gravity variations have very minor impact on the flame. Only low frequency, high amplitude variations affect the flow field in an important manner. The low frequency, high amplitude variations can be identified from accelerometer readings. Thus, only parabolas exhibiting very weak low frequency variations were selected for the subsequent processing. The fine reproducibility of the results eventually supports the interpretation developed in the following.

As mentioned, the rig also allows the conditions to be reproduced at normal gravity on ground. The flame then spreads over a vertical wire while the oxidizer flows upwards.

(a) **(b)**

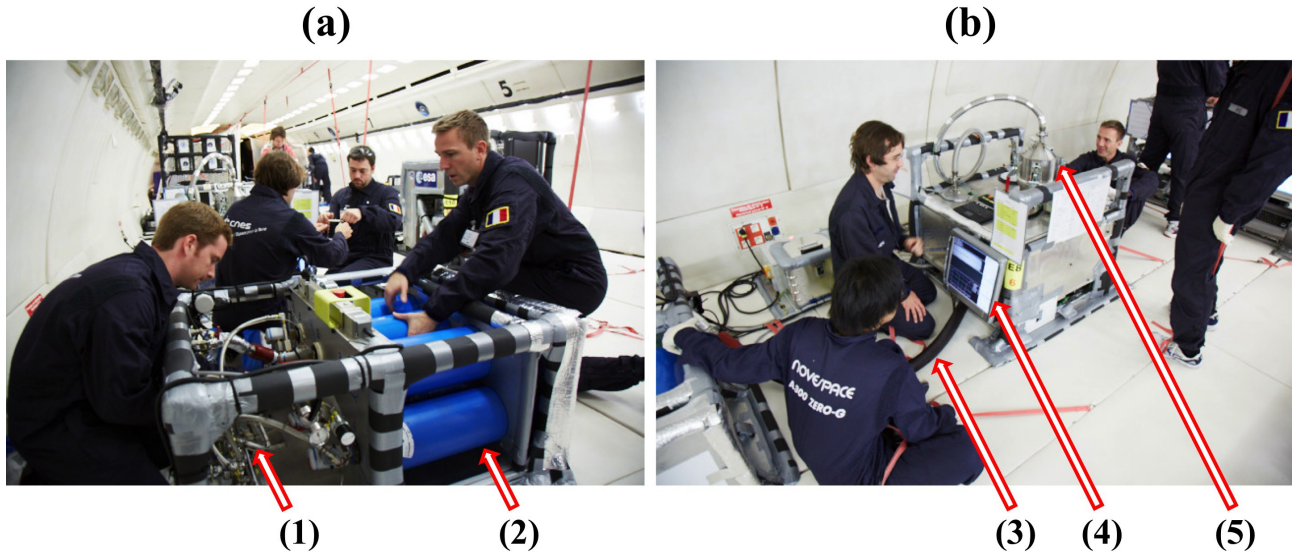**(1)** **(2)** **(3)** **(4)** **(5)**

Figure 4: Pictures of the rig on board the Novespace airplane. (a) Secondary rack dedicated to the oxidizer mixture preparation: (1) cylinders of compressed air and nitrogen; (2) mixing manifold. (b) Main rack: (3) oxidizer line connecting the mixing manifold on the secondary rack to the combustion chamber inlet; (4) data acquisition and control screen; (5) removable top end of the combustion chamber connected to the exhaust line.

III. Characterization of multiple flame spread

The main objective of the present study was to look for conditions that could reveal how flame spread interaction was influenced by the variation in gravity. For this reason, concomitant flame spreads over three parallel wires were investigated, both at normal gravity and in microgravity. The mass burning rates were measured then contrasted with those obtained for single wire flame spreads.

III.1. Sample configuration

Figure 5 (a) shows a schematic of the sample holder to be inserted inside the combustion chamber (see Fig.2). Three parallel wires (4) are shown mounted in the current schematic. Every wire was first cautiously prepared, as shown on the picture of the 1-wire configuration in Fig.5 (b). To do so, every wire leading edge was uncoated so that the coating leading edge was located 20 mm downstream the leading edge rod (2) around which 1 roll of the wire metallic core was made. Hot wire measurements showed that at a distance of 20 mm downstream the leading edge rod, the velocity perturbations due to the rod are very weak within the range of the oxidizer velocity investigated. The wire trailing edge was also uncoated, and then the metallic core was inserted into the hole made through the trailing edge ceramic rod (6). A spring (7) encompassed between this rod

10

and a ceramic cap allowed the wire to be stretched even along flame spread scenarios that tended to make the wire distort due to thermal expansion.

Two consecutive holes in the trailing edge ceramic rod are separated by a distance of 5 mm. Thus, in the 3-wire configuration, the distance between two consecutive wires can be adjusted to 5, 10, or 15 mm.

For the ignition procedure, a 0.25 mm diameter Kanthal wire (3) was wrapped around the leading edge of every coating. Both ends of this wire were tightened between brass nuts. The lateral threaded rods (5) allow the location of these nuts, and therefore also the ignition point, to be shifted along the coating. Thus, both concurrent and opposed flame spread could be conducted alternatively. A 12 V power supply was switched on when the ignition was requested, delivering a current of 5 A that flows in the Kanthal wire, which is connected to the power supply through the plugs (1) that are inserted into slots screwed into the combustion chamber inner walls.
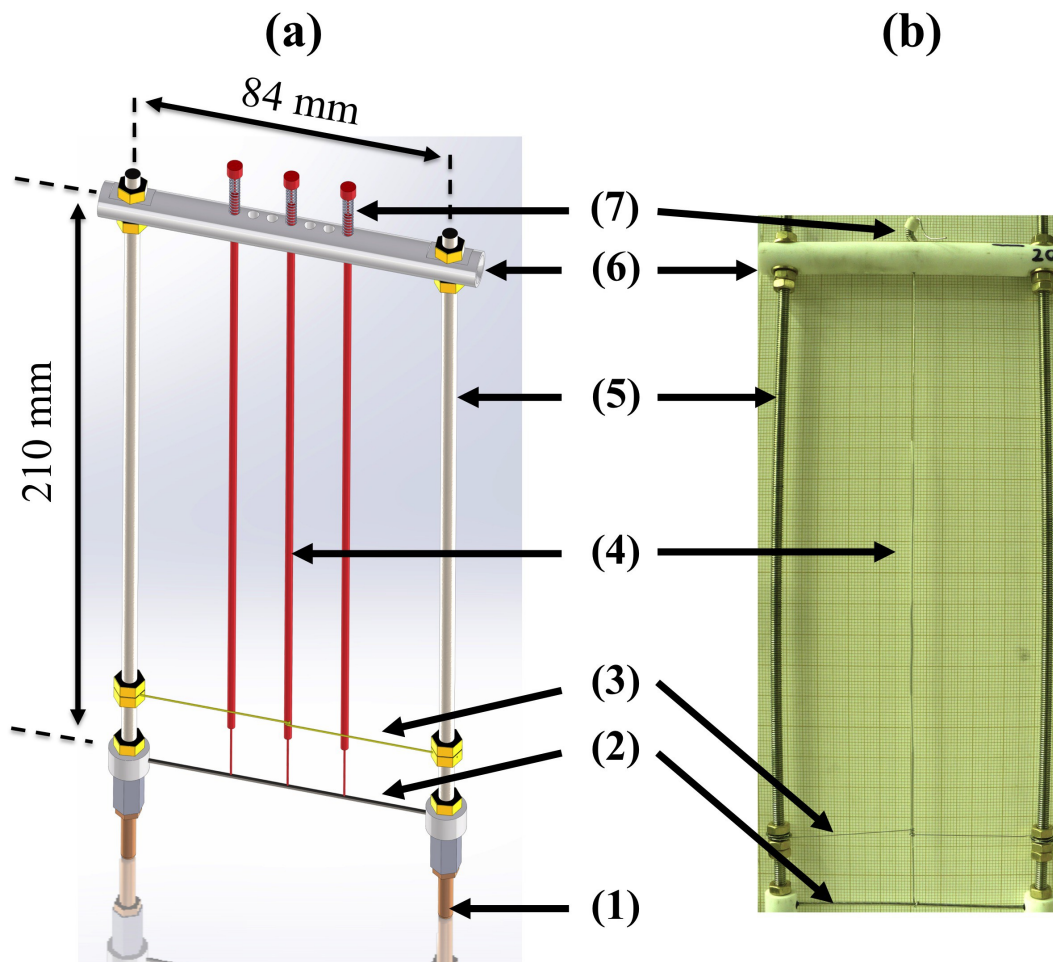
Figure 5: (a) Schematic of the sample holder enabling the 3-wire configuration. (b) Picture of the sample holder with the 1-wire configuration (captured with a wide angle lens). (1) Plug; (2) 1.2 mm diameter stainless steel rod; (3) Kanthal wire; (4) polyethylene coated wire; (5) 4 mm diameter threaded stainless steel rod; (6) 10 mm diameter ceramic rod; (7) stainless steel spring and ceramic cap.

III.2. Operation

The top end of the combustion chamber has been designed to enable its fast opening, closing, and locking. All the four latch clamps (see (4) in Fig.2) have to be handled to this end. In addition, ports allowing the sample holder to be mounted or removed quickly are incorporated into the inner combustion chamber. The aforementioned slots hosting the plugs located at the sample holder leading edge (see (1) in Fig.5) have been shaped to minimize the perturbation of the boundary layer at the wall (see section II.2.). At both ends of the ceramic rod located at the sample holder trailing edge (see (6) in Fig.5), two horizontal ogival beams ensure the rigidity of the assembly when the sample holder is installed inside the chamber. Every ogival beam is connected to the chamber wall through a spring. An operator can push aside the ogival beams, allowing the sample holder to be undocked.

As shown in the video provided as a supplementary material, in between two consecutive parabola, i.e. within a 3 minute long period of time, two operators are then able to open the chamber, remove the used sample holder, insert the one holding the new wire to be burnt, close and lock the chamber, and finally establish the new conditions inside the chamber. Following this procedure, all of the 31 parabolas that a parabolic flight provides can be operated successfully.

III.3. Optical diagnostics and image processing

Four windows enable a large optical access to the combustion chamber (see Fig.2). Every window is 100 mm high, 40 mm wide, and 10 mm thick. All windows are made of 7980 0F fused silica to provide a transmittance higher than 99.5% within a large spectral range spanning from 200 nm to 1300 nm. As shown in Fig.2, the lines-of-sights joining two opposite windows are perpendicular.

Within the framework of the present study, two kinds of visualization are set up to capture the spread from both lines-of-sight simultaneously. To this end, the aforementioned ports that allow the sample holder to be docked have been located so that the angle between any of the lines-of-sight

and the normal to the plane containing the sample holder is 45 degrees.

Not shown in Fig.2, a 10-bit black and white JAI 1600x1200 pixel CCD camera captures the visible flame along its spread over the wire coating. This camera is focused on the plane containing the chamber's axis of symmetry using a Nikor 17-mm f/2.8 lens together with a bandpass filter centered at 650 nm and whose bandwidth at half the transmissivity maximum is of 60 nm. With this optical arrangement, each pixel in the CCD array focused light from a volume corresponding to 0.3 mm in height, 0.3 mm in width and 35 mm in depth without any perturbation due to the light emitted by the LEDs enabling the backlighting technique.

Figure 2 shows the arrangement setting this backlighting technique that enables both the coating regression and the soot particles to be imaged. The light source is provided by a set of LEDs (8) covering an aluminum plate. The current flowing through the LEDs, and therefore the intensity of the backlighting as imaged by the camera can be adjusted. Because the aluminum plate at the back promotes the cooling of the setup, the spectrum of the light emitted by the LEDs does not experience any redshift. This was evidenced by measurements conducted with a spectrometer. A diffusive screen (9) made of polished polycarbonate is inserted between the LEDs and the window to make the backlighting intensity very homogeneous. The backlighting screen is imaged by a 10-bit black and white JAI 1600x1200 pixel CCD camera (7) mounted with a Nikor 17-mm f/2.8 lens together with a bandpass filter centered at 530 nm and whose bandwidth at half the transmissivity maximum is of 20 nm. A typical frame recorded along a flame spread in microgravity is shown on the left hand side of Fig.6. The shadow of the window can be seen on the edges. The intensity distribution of this frame is shown on the right hand side. With these optical settings, the intensity ranges attributed to the wire and its coating on one hand, and to the backlighting screen whose light is potentially partially absorbed by soot on the other hand can be discriminated. Furthermore, each pixel in the CCD array received focused light from a volume corresponding to 0.3 mm in height, 0.3 mm in width and 35 mm in depth.

A digital pulse generator (DG) controls the occurrence and the duration of every CCD exposure, together with the power supply switch of the LEDs. For the present study, the exposure times of the cameras that image the backlighting screen and the visible flame start simultaneously and were set to 10 ms and 20 ms, respectively. Every frame rate was set to 31.5 fps. The LEDs' power supply was switched on every two frames. This provided a sequence of pairs of frames, one imaging the

backlighting together with the flame spontaneous emission, the following one capturing only the flame's spontaneous emission. Subtracting the latter from the former allows the absorption field through the flame to be inferred [27]. The LEDs were switched on 5 ms before the CCD exposure was requested, and were then switched off 5 ms after the CCD exposure was terminated. This prevented the signals delivered by the pixels from being affected by the LEDs transient states. A frame grabber recorded the frames captured by the cameras on the computer that also acquired the other experimental data, i.e. the combustion chamber pressure, the incoming flow rate and temperature, the exhaust flow temperature, and the gravity level. Consequently, all the experimental data can be tracked along a single timeline.

The imaging of the visible flame spread is here used to detect the time of ignition, referred as t=0 in the following. For the 3-wire configuration, t=0 indicates the time of the first detected ignition. The backlighting imaging, on the other hand, allows the coating regression rate to be evaluated. Due to the very bimodal characteristic of the intensity distribution shown in Fig.6, a threshold value between the coated wire and its surrounding can be determined from the intensity distribution for each backlighting frame. The coated wire envelope corresponding to this threshold is then extracted by an edge detection algorithm. The detected envelopes are found to be fairly insensitive to the selected threshold value. Thus, for every frame i, the diameter $d_j^{(i)}$ of the coated wire can be evaluated at every streamwise coordinate z_j along the wire. Assuming that the cylindrical symmetry is conserved and the densities, ρ, of the solid and melted polyethylene coating are very close (0.920 g/cm³), the mass, $m^{(i)}$, of polyethylene can be evaluated for frame i as follows:

$$m^{(i)} = \rho \frac{\pi}{4} \Delta z \sum_{j=1}^{N} \left(\left(d_j^{(i)} \right)^2 - d_m^2 \right)$$

(1)

where $d_m = 0.5$ mm is the diameter of the wire metallic core, $\Delta z = 0.3$ mm the length along the wire that a pixel height represents, and N = 500 the number of lines in the frame.

At the time $t^{(i)}$ when the exposure of frame i starts, the mass burning rate $\dot{m}^{(i)}$ can then be computed:

$$\dot{m}^{(i)} = \frac{m^{(i)} - m^{(i-1)}}{\Delta t}$$

(2)

where $\Delta t = 31.7$ ms is the time between two consecutive frames. In the following, only the potential

14

steady mass burning rate will be commented. As a result, the selection of the backward time step in Eq.(2) will not affect the subsequent findings.

Further information can be extracted from the aforementioned imaging procedure, such as the visible flame standoff distance and the maps of soot volume fraction. While these are crucial characteristics for flame spreads analysis [19,20,28], their interpretations are beyond the scope of the present study.
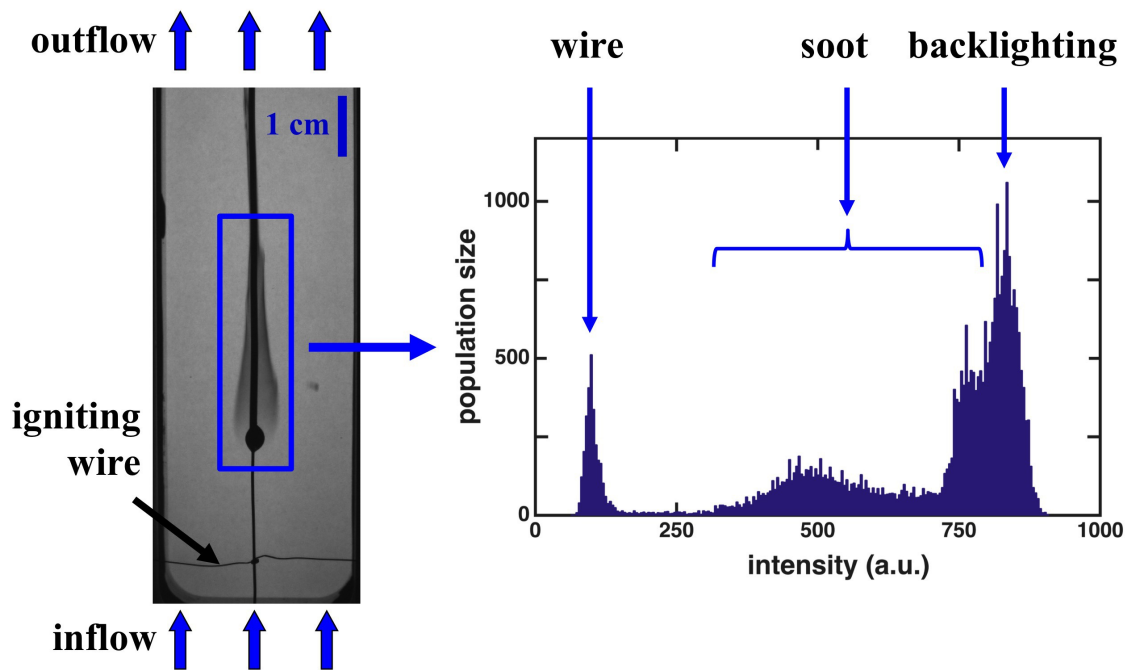

Figure 6: On the left, frame provided by the backlighting technique capturing the flame spread along the polyethylene coating of a wire in microgravity for V_{OX}=5 cm/s. On the right, distribution of the intensities delivered by the pixels encompassed within the region delineated by the blue rectangle drawn on the frame.

15

III.4. Multiple flame spread

Figure 7 shows a selection of frames recorded by the backlighting technique along the concomitant spreads over three wires in microgravity. A lens with a short focal length (17 mm) was required to capture the spreads within the field of view. For this reason, this distortion of the wire-assembly that arose from the aforementioned angle between the line-of-sight and the normal to the plane containing the sample holder was amplified with the streamwise coordinate, z, as shown by the slope of the white dotted lines in Fig.7. A photograph of a very accurate grid before every flight allowed every frame to be corrected for this distortion.

The conditions set to conduct the spreads imaged by Fig.7 are an air flow velocity $V_{OX} = 5$ cm/s $\pm$ 0.1 cm/s, a pressure of 1 atm $\pm$ 0.01 atm, an inflow temperature of 298K $\pm$ 1K, and a spacing between two consecutive wires of 15 mm $\pm$ 1mm. To delay the ignition of the central wire coating, four and five wraps of igniting wire were made around the central wire and the lateral ones, respectively. During the ignition procedure (5s), the energy deposited was about 20% lower on the central wire than in the lateral ones. As a result, the spread over the central wire's coating was delayed, as shown on the frame captured at t = 4.35 s (Fig.7).

Two opposite trends may be revealed due to the potential interaction among these flame spreads. The reduced energy deposited on the central wire coating and the oxygen dilution by the combustion products released by the lateral flames would tend to magnify the initial spread delay. Contrarily, the preheating of the central wire coating by the heat released by the lateral flames may accelerate the central spread. As shown by the sequence of frames in Fig.7, the latter effect governs the interaction of spreads in microgravity for the conditions established.

Due to the limited number of parabolas, only two identical tests could be conducted in microgravity. Still, both unveiled the same tendency. Identical conditions could then be established on ground, and for the ten tests conducted at normal gravity, no central spread could catch up with the lateral ones. Although a further theoretical analysis is now required, one can decently speculate that the upward convection at normal gravity magnified due to the fact that buoyancy can partially sweep away the heat released by the lateral flames, and thereby weaken the preheating of the coating. Conversely, in microgravity, radiative transfer - partially directed to the coating - is amplified, especially due to increased residence times in flames [29] and enhanced soot production [30]. As a result, spreading flames established in microgravity may interact at longer length scales that at normal gravity.
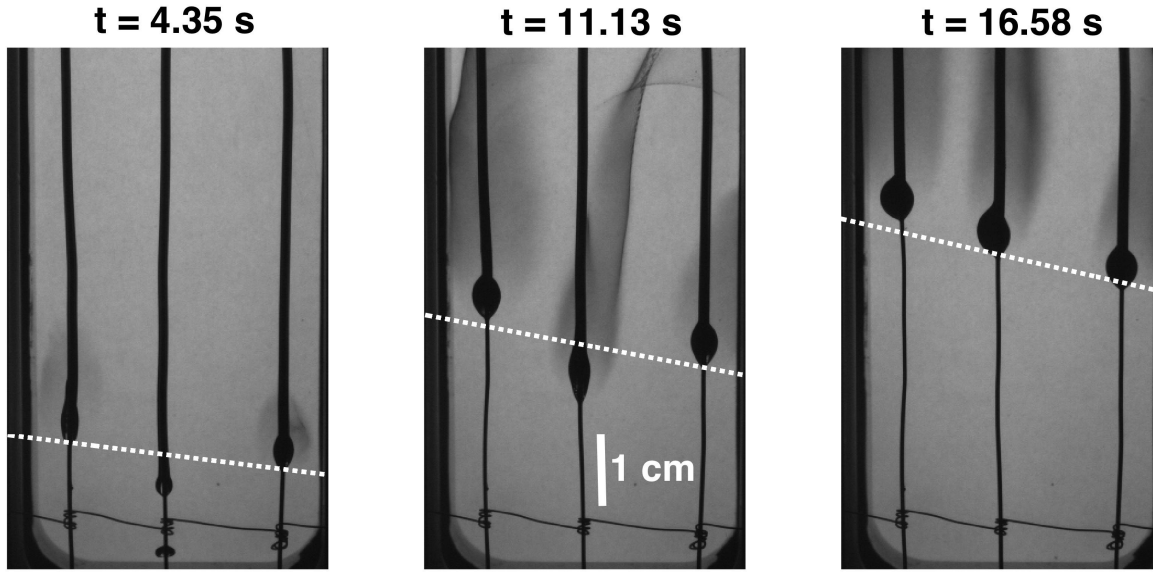
Figure 7: Sequence of frames recorded along the concomitant spreads over three wires in microgravity for V_{OX}=5 cm/s. t = 0 is the time when the first wire ignition can be detected. The white dotted lines indicate the location of iso-streamwise coordinate z. The delay between the lateral ignitions and the central one is about 4s.

Figure 8 exhibits the time histories of the concomitant coating mass burning rates $\dot{m}$ along a test conducted at identical conditions, either in microgravity (on the left) or at normal gravity (on the right), for an air flow velocity V_{OX} = 5 cm/s. Wires 1, 2 and 3 are the left, central, and right wires shown in Fig.7, respectively. The subscripts following $\dot{m}$ and the brackets indicate the number of wires burning concomitantly and the gravity condition, respectively. $\dot{m}_1^{st}$ is the mass burning rate measured when the spread over a single wire becomes steady. For microgravity and normal gravity, the values of $\dot{m}_1^{st}$ are 41 mg/s and 202 mg/s, respectively. These have been averaged over three and ten tests, respectively. As already evidenced in the literature [31], buoyancy tends to accelerate the burning rates of upward flame spread over a single vertical wire.

In Fig.8, the shaded areas represent the range of steady mass burning rates of a single wire scaled by the value $\dot{m}_1^{st}$ .averaged over these steady rates. The range width is lower than 8% for the rates measured in microgravity while it is of 19% for those measured at normal gravity. Indeed, the time histories of raw mass burning rates measured at normal gravity appear more bumpy due to possible

melted polyethylene drops falling along the wires at normal gravity (see the quite scattered dots on the right in Fig.8).

For this reason, trends shown by the solid lines in Fig.8 are extracted when averaging the raw mass burning rates over the ten preceding measurements, i.e. a 320 ms long period of time. The following analysis is hardly affected by the selected value of this period.

For the rates measured in microgravity, the timeline stops at the end of the microgravity period (about 22s) as the integrity of the coating trailing edge still remains at this time. For the rates measured at normal gravity, the timeline stops when the trailing edge of the burning coating starts being damaged. While the characteristic time of the transient spread leading to the steady state is significantly lower at normal gravity, the trends exhibited by the mass burning rates are very similar at both levels of gravity. After a slow increase, every mass burning rate experiences a significant acceleration before reaching a steady rate. The acceleration over wire 2 is delayed at both gravity conditions. However, the steady mass burning rate of wire 2 is 18% higher than the one exhibited by the spread over a single wire in microgravity. Concomitantly, the steady mass burning rates of wires 1 and 3 remain within the upper range of the rates measured for the single wire. On the opposite, all the three steady mass burning rates measured at normal gravity eventually fall into the range of rates exhibited by the spread established over a single wire. Thus, the interaction among flame spreads is here quantitatively unveiled in microgravity while it cannot be evidenced for the identical conditions at normal gravity.
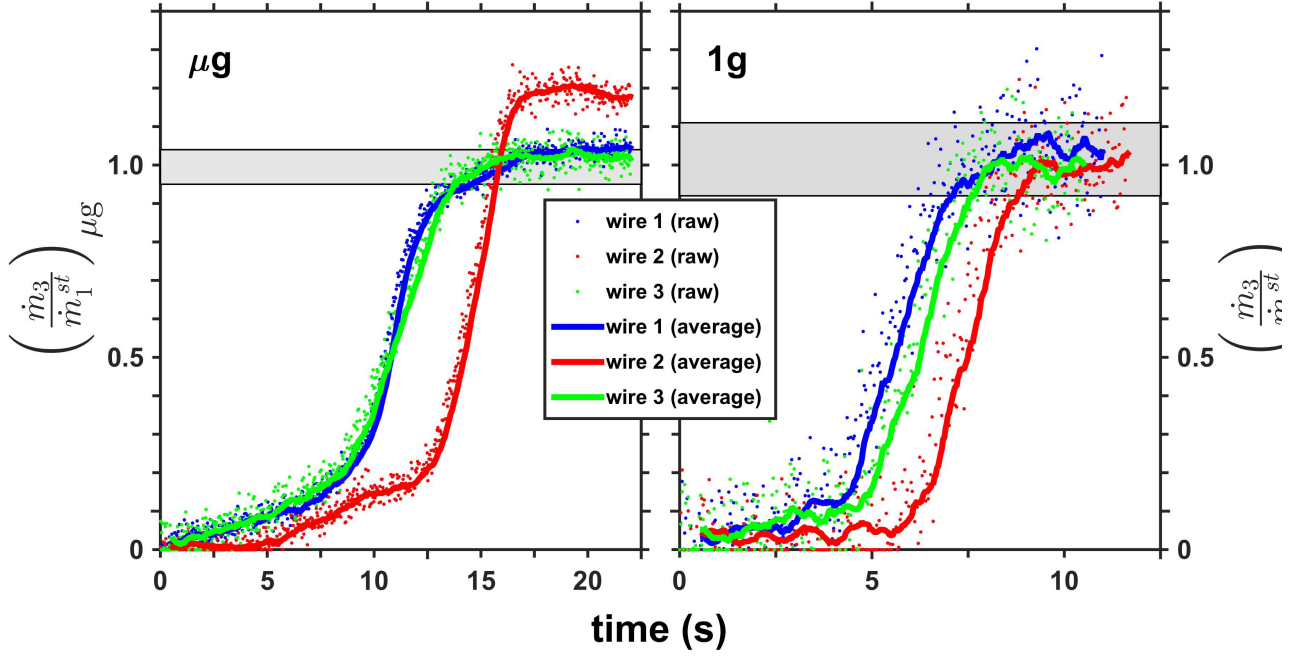
Figure 8: Time histories of the three concomitant coatings mass burning rates, in microgravity on the left and at normal gravity on the right, for V_{OX}=5 cm/s. Every burning rate $\dot{m}_3$ is scaled by the mean steady burning rate $\dot{m}_1^{st}$ measured along the spread over a single wire, either in microgravity on the left or at normal gravity on the right. The shaded areas represent the range of $\dot{m}_1^{st}$ measured for both gravity conditions. The dots indicate the instantaneous mass burning rates while the lines represent the rates averaged over the ten preceding measurements.

IV. Conclusion

A new rig was custom-designed to allow for a study of concomitant flame spread established over the coatings of electrical wires in microgravity. The rig was specifically designed for experiments to be conducted in parabolic flights. Special attention was given to the characterization of the inner combustion chamber aerodynamics. For the configuration studied, the coatings burned concomitantly in a steady uniform laminar air flow. A backlighting technique was set up to capture the coatings mass burning rates from quantified surface regression.

To highlight the interaction among flame spreads in microgravity, three parallel wires burned concomitantly. Ignition on the central coating was delayed. During the microgravity period, the central flame caught up with the lateral ones. As a result of the aforementioned interaction, the steady mass burning rate measured over the central wire in microgravity revealed a non-ambiguous increase as compared to the steady rate measured over a single wire. Interestingly, this interaction could not be observed for the similar configuration at normal gravity. The present results show

significant changes in heat exchange between wires and the resulting influence on flame spread, nevertheless, detailed quantification of what induces these changes requires further theoretical and experimental investigation.

References

[1] P.S. Greenberg, K.R. Sacksteder, T. Kashiwagi, The USML-1 wire insulation flammability glovebox experiment, Third International Microgravity Combustion Workshop 2, NASA Lewis Research Center, Cleveland, Ohio, April 11-13, 1994, p.25-30.

[2] R. Friedman, Fire safety in the low-gravity space- craft environment, National Aeronautics and Space Administration, Glenn Research Center, 1999.

[3] V. Babrauskas, Ignition Handbook Database, Fire Science Publishers, 2003.

[4] R. Friedman, Fire Safety in Spacecraft, Fire Mater. 20 (1996) 235-243.

[5] M. Kikuchi, O. Fujita, K. Ito, A. Sato, T. Sakuraya, Experimental study on flame spread over wire insulation in microgravity, Proc. Combust. Inst. 27 (1998) 2507-2514.

[6] O. Fujita, M. Kikuchi, K. Ito, K. Nishizawa, Effective mechanisms to determine flame spread rate over ethylene-tetrafluoroethylzene wire insulation: Discussion on dilution gas effect based on temperature measurements, Proc. Combust. Inst. 28 (2000) 2905-2911.

[7] O. Fujita, K. Nishizawa, K. Ito, Effect of low external flow on flame spread over polyethylene-insulated wire in microgravity, Proc. Combust. Inst. 29 (2002) 2545–2552.

[8] Y. Onishi, O. Fujita, K. Agata, et al., Observation of Flame Spreading over Electric Wire under Reduced Gravity Condition Given by Parabolic Flight and Drop Tower Experiments, JSASS Aerospace Tech. Japan 8 (ists27) (2010) Ph_19– Ph_24.

[9] A. Umemura, M. Uchida, T. Hirata, J. Sato, Physical model analysis of flame spreading along an electrical wire in microgravity, Proc. Combust. Inst. 29 (2002) 2535-2543.

[10] Y. Nakamura, N. Yoshimura, H. Ito, K. Azumaya, O. Fujita, Flame spread over electric wire in sub-atmospheric pressure, Proc. Combust. Inst. 32 (2009) 2559–2566.

[11] J. Torero, Scaling-Up fire, Proc. Combust. Inst. 34 (2013) 99–124.

[12] O. Fujita, Solid combustion research in microgravity as a basis of fire safety in space, Proc. Combust. Inst. 35 (2015) 2487–2502.

[13] G. Jomaas, J.L. Torero, C. Eigenbrod, J. Niehaus, S.L. Olson, P.V. Ferkul, G. Legros, A.C. Fernandez-Pello, A.J. Cowlard, S. Rouvreau, N. Smirnov, O. Fujita, J.S. T'ien, G.A. Ruff, D.L. Urban, Fire safety in space – beyond flammability testing of small samples, Acta Astronautica 109 (2015) 208–216.

[14] S.L. Olson, Radiative Exchange during Concurrent Flame Spread over Three Parallel Thin Fuel Sheets in Microgravity, Spring Technical Meeting of the Central States Section of the Combustion Institute, March 16-18, 2014.

[15] C.M. Megaridis, B. Konsur, D.W. Griffin, Soot-Field Structure in Laminar Soot-Emitting Microgravity Non-Premixed Flames, Proc. Combust. Inst. 26 (1996) 1291-1299.

[16]   W. Kong, F. Liu, Numerical study of the effects of gravity on soot formation in laminar coflow methane/air diffusion flames unde different air stream velocities, Combust. Theory Model. 13 (2009) 993-1023.

[17]   S.L. Olson, J.S. T'ien, Buoyant low-stretch diffusion flames beneath cylindrical PMMA samples, Combust. Flame 121 (2000) 439-452.

[18]   S. Rouvreau, P. Cordeiro, J.L. Torero, P. Joulain, Influence of the G-Jitter on a laminar boundary layer type diffusion flame, Proc. Combust. Inst. 30 (2005) 519-526.

[19]   A. Fuentes, G. Legros, A. Claverie, P. Joulain, J.-P. Vantelon, J.L. Torero, Interactions between soot and CH* in a laminar boundary layer type diffusion flame in microgravity, Proc. Combust. Inst. 31 (2007) 2685-2692.

[20]   G. Legros, A. Fuentes, S. Rouvreau, P. Joulain, B. Porterie, J.L. Torero, Transport mechanisms controlling soot production inside a non-buoyant laminar diffusion flame, Proc. Combust. Inst. 32 (2009) 2461-2470.

[21]   H. Emmons, The film combustion of liquid fuel, Z. Angew. Math. Mech. 36 (1956) 60.

[22]   F.J. Kosdon, F.A. Williams, C. Buman, Combustion of vertical cellulosic cylinders in air, Proc. Combust. Instit. 12 (1968) 253-264.

[23]   P.J. Pagni, T.M. Shih, Excess pyrolyzate, Proc. Combust. Instit. 16 (1978) 1329-1343.

[24]   K. Anamalai, M. Sibulkin, Flame spread over combustible surfaces for laminar flow systems, Combust. Sci. Technol. 19 (1979) 167-183.

[25]   J.S. T'ien, H. Shih, C. Jiang, H.D. Ross, F.J. Miller, A.C. Fernandez-Pello, J.L. Torero, D.C. Walther, "Mechanisms of Flame Spread and Smolder Wave Propagation," Microgravity Combustion: Fire in Free Fall, H.D. Ross (Editor), Academic Press, 299-417, 2001.

[26]   http://www.ansys.com/Products/Fluids/ANSYS+Fluent

[27]   M. Kashif, J. Bonnety, P. Guibert, C. Morin, G. Legros, Soot volume fraction fields in unsteady axis-symmetric flames by continuous laser extinction technique, Opt. Express 20 (2012) 28742-28751.

[28]   G. Legros, A. Fuentes, J. Baillargeat, P. Joulain, J.P. Vantelon, J.L. Torero, Three-Dimensional Recomposition of the Absorption Field Inside a Non-Buoyant Sooting Diffusion Flame, Opt. Lett. 30 (2005) 3311-3313.

[29]   A. Fuentes, S. Rouvreau, P. Joulain, J.-P. Vantelon, G. Legros, J.L. Torero, A.C. Fernandez-Pello, Sooting behavior dynamics of a non-buoyant laminar diffusion flame, Combust. Sci. Technol. 179 (2007) 3-19.

[30]   G. Legros, J.L. Torero, Phenomenological model of soot production inside a non-buoyant laminar diffusion flame, Proc. Combust. Inst. 35 (2015) 2545-2553.

[31]   L. Hu, Y. Zhang, K. Yoshioka, H. Izumo, O. Fujita, Flame spread over electric wire with high thermal conductivity metal core at different inclinations, Proc. Combust. Inst. 35 (2015) 2607-2614.